Chemical Geology 559 (2021) 119910

Contents lists available at ScienceDirect

Chemical Geology

journal homepage: www.elsevier.com/locate/chemgeo

# Mercury and sulfur isotopic composition of sulfides from sediment-hosted lead-zinc deposits in Lanping basin, Southwestern China

Yue-Fu Liu[a,b], Hua-Wen Qi[a,*], Xian-Wu Bi[a,*], Rui-Zhong Hu[a], Lin-Kun Qi[c], Run-Sheng Yin[a], Yong-Yong Tang[a]

[a] State Key Laboratory of Ore Deposit Geochemistry, Institute of Geochemistry, Chinese Academy of Sciences, Guiyang 550081, China
[b] University of Chinese Academy of Sciences, Beijing 100049, China
[c] No. 310 Geological Team of Yunnan Nonferrous Geological Bureau, Dali 671000, China

ARTICLE INFO

Editor: Michael E. Boettcher

*Keywords:*
Mercury isotope
Sulfur isotope
Pb-Zn deposits
Lanping basin
Southwestern China

ABSTRACT

The Lanping basin is an important Pb-Zn-Cu-Ag polymetallic province in southwestern (SW) China. Mineralization types in the basin include mainly MVT Pb-Zn deposits, vein-type Cu deposits, and minor quartz vein-type Pb-Zn deposits. In this study, we analyzed the total Hg (THg) content and Hg-S isotopic compositions of sulfides from two types of Pb-Zn deposits in the basin, and investigate the Hg isotope fractionation mechanism and its major controlling factors in the Pb-Zn ore-forming process. At the Shangnuluo quartz vein-type Pb-Zn-Sb deposit, sulfides (especially sphalerite) show a wide $\delta^{202}$Hg range (−0.40 to 2.71‰), suggesting that $Hg^0$ evaporation from hydrothermal fluids occurred during the ore formation. Negative THg vs. $\delta^{202}$Hg correlation in the sphalerites suggests a mixing of Hg from the vapor phase (low $\delta^{202}$Hg, high THg) and the residual aqueous phase (high $\delta^{202}$Hg, low THg). The negative $\Delta^{199}$Hg (−0.42 to −0.08‰) suggests that the Hg was sourced from the metamorphic basement, whereas the negative $\delta^{34}$S values (−13.0 to −2.7‰) suggests that the sulfur was mainly sourced from sedimentary sequences, possibly related to the organic matter decomposition and thermochemical sulfate reduction (TSR). For the Liziping and Fulongchang MVT Pb-Zn deposits, sulfides have relatively narrow $\delta^{202}$Hg range (−1.46 to 0.25‰), suggesting limited $Hg^0$ evaporation during the mineralization. Lower $\delta^{202}$Hg values were observed in the early-stage sulfides from these two deposits, probably due to the preferential precipitation of lighter Hg isotopes in these early-stage sulfides. Sulfides from both deposits have negative $\Delta^{199}$Hg values (−0.24 to 0.01‰), suggesting that the Hg was also derived from the metamorphic basement. Sulfide $\delta^{34}$S values from the two deposits are positive, which also suggests that the sulfur was sourced from sedimentary sequences, but mainly related to TSR under relatively low-temperatures. Sulfides from different Pb-Zn deposit types in the Sanjiang Tethyans Metallogenic Belt fall into distinct fields in the $\delta^{34}$S vs. $\delta^{202}$Hg (or $\Delta^{199}$Hg) diagrams, indicating that the integration of S and Hg isotopes is useful to discriminate different types of Pb-Zn deposits.

## 1. Introduction

The Lanping basin is a typical Mesozoic-Cenozoic intracontinental basin, situated in the tectonic junction between the Eurasia and Indian plates. This basin is located in the central part of the Sanjiang Tethyan metallogenic belt (STMB) (Hou et al., 2007; He et al., 2009; Deng et al., 2014; Bi et al., 2019), bordered with the Simao basin in the south and gradually thins out in the north (Fig. 1a). The Proterozoic metamorphic basement in the Lanping basin is exposed outside the basinal faults, whilst exposed sedimentary sequences in the basin comprise mainly Cenozoic terrigenous red clastic rocks. Cenozoic magmatic rocks are only exposed in the southern margin and periphery of the basin. The basin is well endowed with various types of ore deposits, which constitute an important Pb-Zn polymetallic province in southwestern (SW) China (Hou et al., 2007; He et al., 2009; Deng et al., 2014; Bi et al., 2019). Ore deposits in the basin have been interpreted to belong to two metallogenic systems: A vein-type (commonly quartz veins) Cu system (e.g., Jinman, Liancheng, Kedengjian; Zhang et al., 2013, 2015); and a MVT or basinal brine-related Pb-Zn-(Cu-Ag) system (e.g., large Jinding and Baiyangping orefields) (Chen et al., 2004; Xue et al., 2007; Feng et al., 2014; Tang et al., 2014, 2017; Zou et al., 2015; Wang et al., 2015; Bi et al., 2019).

* Corresponding authors.
*E-mail addresses:* qihuawen@vip.gyig.ac.cn (H.-W. Qi), bixianwu@vip.gyig.ac.cn (X.-W. Bi).

https://doi.org/10.1016/j.chemgeo.2020.119910
Received 4 September 2019; Received in revised form 24 September 2020; Accepted 1 October 2020
Available online 09 October 2020

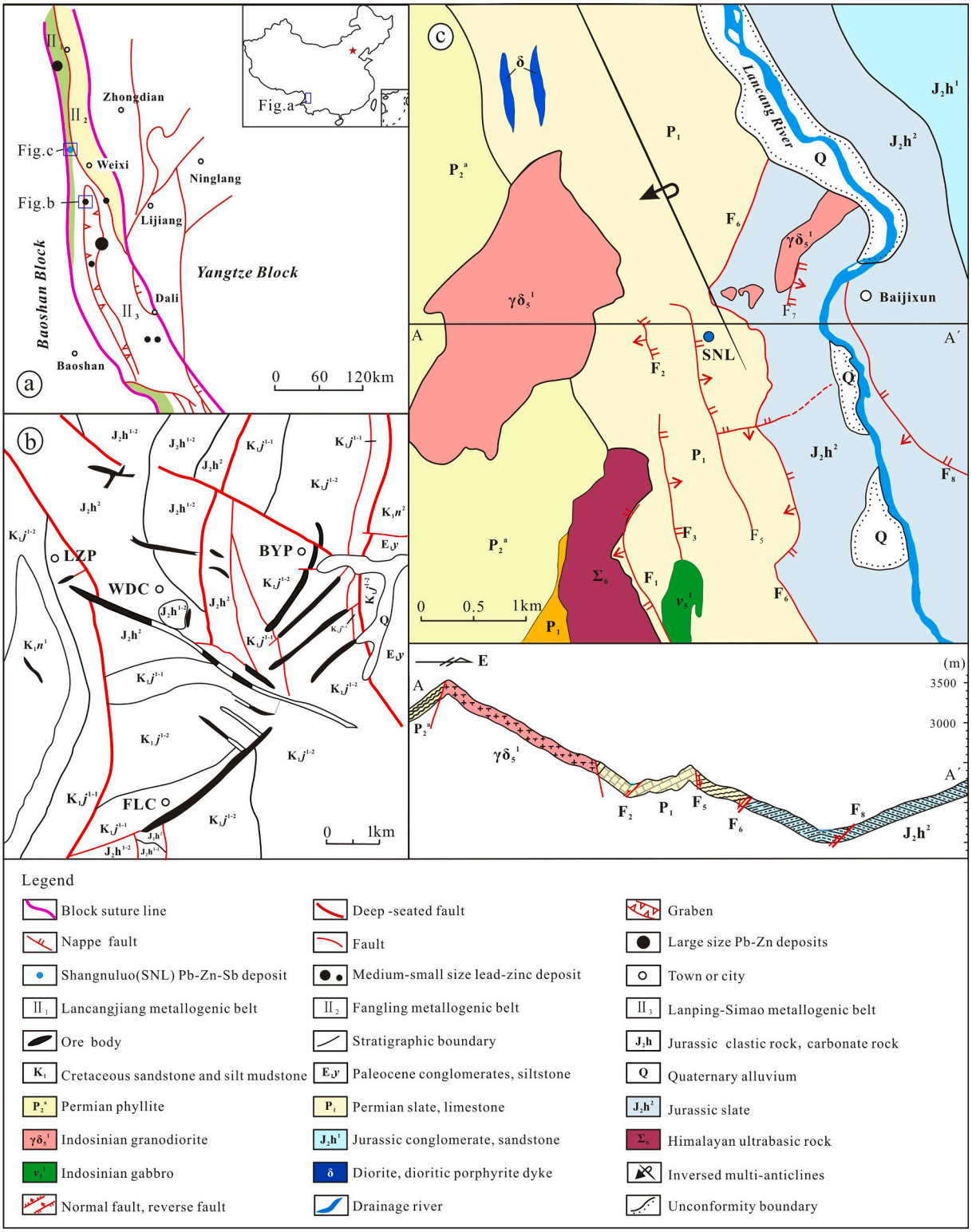


**Fig. 1.** Simplified tectonic/geologic map of the northern margin of Lanping basin. (a) Lanping basin (modified after Zhang et al., 2009); (b) Liziping and Fulongchang Pb-Zn deposits (modified after Wang et al., 2015; Zou et al., 2015); (c) Shangnuluo Pb-Zn-Sb deposit (this study).

In the last two decades, geological studies in the Lanping basin were mainly focused on the ore-fluid nature, calcite/quartz REEs and C-H-O isotopes, and sulfide S-Pb isotopes (Xue et al., 2007; Zhang et al., 2013; Feng et al., 2014; Tang et al., 2014; Wang et al., 2015 and reference therein), fluid inclusion (FI) He-Ar isotopes (Xue et al., 2007; Zhang et al., 2015; Tang et al., 2017), molybdenite Re-Os, sphalerite/galena Rb-Sr and calcite Sm-Nd dating (Zhang et al., 2013; Zou et al., 2015; Bi et al., 2019), space-time distributions and regional geotectonic evolution of the typical deposits in the STMB (Hou et al., 2007; He et al., 2009; Deng et al., 2014; Zhang et al., 2015). However, due to the complex ore-forming processes (multi-source ore-fluid mixing; Bi et al., 2019) and the often ambiguous interpretations on C-H-O-Pb isotopic data, currently the genetic type (especially Jinding, e.g., Jinding type, Xue et al., 2007; MVT, Deng et al., 2014; sub-type of MVT, Leach et al.,

2017) and ore metal/fluid source (mantle vs. crustal or meteoric water; Xue et al., 2007; Tang et al., 2017) of many deposits in this basin remain controversial. In recent years, new types of deposits were continuously discovered in the STMB, e.g., quartz vein-type Zn-Pb-Sb deposits, and the current understanding on their ore-forming process is very limited. Therefore, we attempted to use non-traditional isotopic system (e.g., Hg isotopes) as a new tool to understand the potentially different Pb-Zn ore-forming processes in the Lanping basin, which would likely benefit the regional metallogenic research and exploration.

Mercury (Hg) is a redox sensitive metal with strong mobility and biotoxicity (Lamborg et al., 2003). During Hg biogeochemical cycling, Hg isotopes can undergo both mass-dependent (Hg-MDF) and mass-independent fractionation (Hg-MIF) (reviewed by Blum et al. (2014)). Hg-MDF occurs during various processes such as $Hg^{II}$ reduction (Kritee et al., 2007, 2009), $Hg^{II}$ adsorption (Wiederhold et al., 2010; Jiskra et al., 2012), bioaccumulation (Laffont et al., 2009, 2011), methylmercury (MeHg) photodegradation and $Hg^{II}$ photoreduction (Bergquist and Blum, 2007; Zheng and Hintelmann, 2009) as well as $Hg^0$ photooxidation (Sun et al., 2016). Hg-MIF only occurs in a few specific processes such as MeHg photodegradation and $Hg^{II}$ photoreduction (Bergquist and Blum, 2007; Zheng and Hintelmann, 2009), $Hg^{II}$-Thiol complexation and $Hg^0$ evaporation (Estrade et al., 2009; Ghosh et al., 2013). $\Delta^{199}Hg/\Delta^{201}Hg$ ratios can be used to define whether Hg-MIF is induced by photochemical reactions or by other processes (reviewed by Sonke, 2011; Blum et al., 2013, 2014). With the observation of distinct Hg isotopic composition in different reservoirs on Earth, scientists have used Hg isotopes as a robust tracer to understand the source and processes of Hg in modern ecological systems (Bergquist and Blum, 2007; Estrade et al., 2010; Feng et al., 2010; Sonke et al., 2010; Yin et al., 2010; Chen et al., 2012, 2016; Blum et al., 2013, 2014; Gleason et al., 2017). Recent studies also used Hg isotopes as an indicator to understand Hg source changes during large igneous province (LIP) events and oceanic anoxic events (OAEs) during geological history (e.g., Sanei et al., 2012; Grasby et al., 2013; Percival et al., 2015; Thibodeau et al., 2016; Shen et al., 2019; Them et al., 2019; Wang et al., 2019).

The application of Hg isotopes in hydrothermal metallogenic studies remains an emerging topic of research. Smith et al. (2005) for the first time reported large variations of $\delta^{202}Hg$ (−3.5 to 2.1‰) in two fossil hydrothermal systems in Nevada, USA, demonstrating that large Hg-MDF could occur during ore-forming fluid boiling. A following Smith et al. (2008) also reported large range of $\delta^{202}Hg$ (−3.69 to 0.67‰) in Hg deposits in California Coast Ranges, USA. They further demonstrated that the variation of $\delta^{202}Hg$ was caused by ore-forming fluid boiling, and the mobilization of Hg from source rocks actually induced limited Hg-MDF (< 0.5‰ in $\delta^{202}Hg$). Sherman et al. (2009) investigated the isotopic composition of Hg in hydrothermal precipitates in the Yellowstone Plateau volcanic field and vent chimney samples from the Guaymas Basin seafloor rift, and hypothesized that mantle Hg is characterized by $\delta^{202}Hg$ of ~0‰ and $\Delta^{199}Hg$ of ~0‰. Zambardi et al. (2009) studied the isotopic signature of volcanic Hg in Vulcano Island, Italy, and demonstrated $\delta^{202}Hg$ of −1.74–0.01‰ and $\Delta^{199}Hg$ of ~0‰. A few studies reported a large variation of $\delta^{202}Hg$ (~5‰) and $\Delta^{199}Hg$ (~0.4‰) in Hg-rich sulfides in Pb-Zn deposits worldwide (Sonke et al., 2010; Yin et al., 2016; Tang et al., 2017), suggesting Hg-MDF or Hg-MIF occurred during the formation of these deposits. However, an increase body of literature suggests that the Hg-MIF signals in hydrothermal deposits are more likely reflective of a contribution of Hg from sedimentary rocks, as Hg-MIF signals in natural samples are mainly found in Earth's surface reservoirs (Yin et al., 2016; Xu et al., 2018). Zhu et al. (2020) reported the total Hg content and Hg isotopic composition ($\delta^{202}Hg$: −1.23 to −0.05‰, $\Delta^{199}Hg$: −0.10 to 0.20‰) of sulfides from two large hydrothermal fields in the Southwest Indian Ridge.

To date, the variation of Hg isotopic composition in hydrothermal deposits is commonly explained by fluid boiling that incudes Hg-MDF or a mixing of Hg from different sources with distinct Hg isotope signals (Yin et al., 2016; Xu et al., 2018). However, there is still a lack of systematic study focusing on sulfide Hg isotope variation in a same deposit or different deposits within a same region. It is noteworthy that substantial amount of Hg isotopic data have been published for the Pb-Zn deposits in the STMB (Tang et al., 2017; Xu et al., 2018), yet comparative studies are still lacking between different deposits. For this reason, we studied the Shangnuluo quartz vein-type Pb-Zn-Sb deposit, and Liziping and Fulongchang MVT Pb-Zn deposits in the Lanping basin. We analyzed the total Hg content and Hg-S isotopes of the coexisting sulfides in these deposits, and discussed the ore-forming fluid/material source and metallogenic mechanism of the two different types of Pb-Zn deposits in the region. Through comparing with other typical Pb-Zn deposits (e.g., Jinding, Cuona, Lanuoma) in the STMB, we assessed the potential of integrating Hg-S isotopes to discriminate various genetic types of Pb-Zn deposits.

## 2. Deposit geology and sampling

### 2.1. Liziping and Fulongchang MVT deposits

The two deposits are located in the western part of the Baiyangping polymetallic orefield, in the northern margin of the Lanping basin. Exposed stratigraphy in the orefield is mainly Mesozoic-Cenozoic, including the Jurassic Huakaizuo Formation (Fm.) (upper member) ($J_2h$) multi-colored clastic and carbonate rocks, (lower member) red clastic rocks (with gypsum bed), Cretaceous Jingxing Fm. ($K_1n$) purplish-red, greyish-white/green quartz sandstone and silty mudstone interbeds (partly greyish-green conglomerate), Nanxing Fm. ($K_1j$) lacustrine purplish-red sandstone, sandy conglomerate, mudstone and siltstone, and the Paleocene Yunlong Fm. ($E_1y$) (Wang et al., 2015, and reference therein).

Ore hosts at Liziping comprise mainly the mudstone and fossiliferous limestone of the Huakaizuo Formation (upper member) ($J_2h^2$), and minor the fossiliferous limestone of the Upper Cretaceous Jingxing Formation. Mineralization at Liziping was mainly controlled by NW-trending strike-slip faults, and the orebodies occur as veins along these faults. The ores appear mainly as veins, disseminations or breccias (Fig. S1a–d). Metallic minerals include mainly sphalerite, gratonite and galena, and minor realgar, orpiment, arsenian pyrite (concentric), chalcopyrite, tetrahedrite, chalcocite and arsenopyrite. Non-metallic minerals include mainly anhydrite, and minor barite, dolomite, ankerite and quartz. Under the microscope, sphalerite is replaced by gratonite, and sphalerite and gratonite are replaced by arsenian pyrite, which also appear as veinlets filling in sphalerite fractures (Fig. 2a–c). This indicates that sphalerite formed before gratonite, and gratonite before arsenian pyrite.

Ore hosts at Fulongchang comprise mainly Lower Cretaceous Jingxing Fm. calcareous sandstone, and minor Middle Jurassic Huakaizuo Fm. limestone and marl. Mineralization at Fulongchang is controlled by the NE-trending Fulongchang fault, and the orebodies appear as vein-type, stratabound and fault-bound lenses. The Pb-Zn-Cu ores appear mainly as massive, breccias and veinlets (Fig. S1e–h). Metallic minerals include mainly sphalerite, galena, jordanite, tetrahedrite and acrusite, and minor boumonite, chalcopyrite, argentite and kongsbergite. Under the microscope, euhedral fine-grained pyrite is included in sphalerite and jordanite, and jordanite replaced sphalerite (Fig. 2d–e). Non-metallic minerals include mainly calcite and locally barite (replaced by sphalerite) (Fig. 2f).

The Liziping and Fulongchang deposits were interpreted to share similar ore-fluid features, including temperature (120–180 °C) and salinity (0.35–24.2 (average 16.9) wt% NaCl eqv.), density (0.84–1.11 g/cm$^3$), suggesting a low-temperature high-salinity basinal brine nature. Also, the fluids contain relatively high oxygen fugacity ($\log f_{O2}$ = −0.878–0.583, average −0.719) and weakly acidic pH (4.95–5.73). Sphalerite Rb-Sr dating and ore-stage calcite Sm-Nd dating

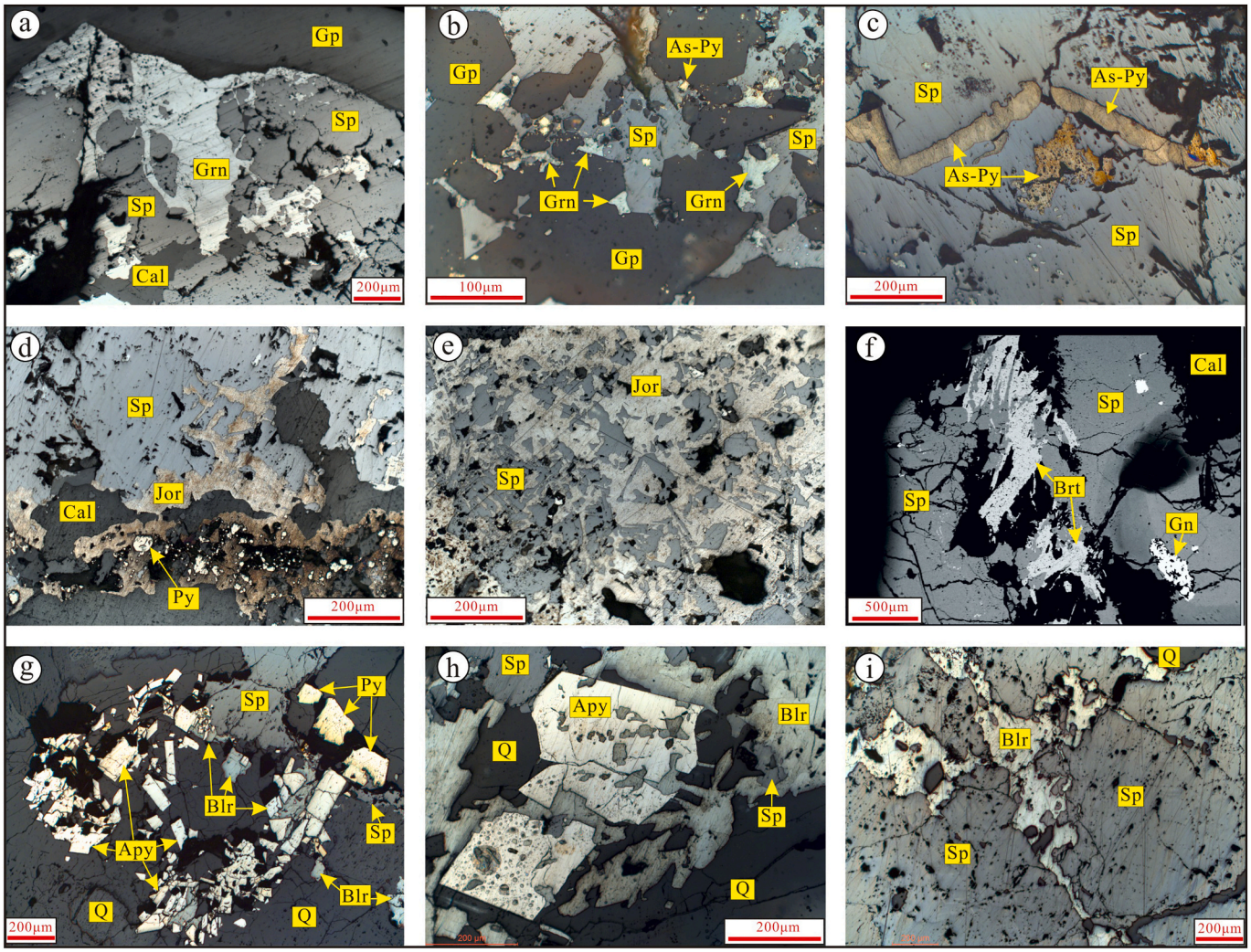


**Fig. 2.** Ore microscopic photos and BSE images from two types of Pb-Zn deposits in the northern margin of Lanping basin: a–c. Liziping deposit; d–f. Fulongchang deposit; g–i. Shangnuluo deposit. Abbreviations: Grn-gratonite; Sp-sphalerite; Gp-gypsum; As-Py-arsenian pyrite; Py-pyrite; Jor-jordanite; Gn-galena; Brt-barite; Blr-boulangerite; Apy-arsenopyrite; Cal-calcite; Q-quartz.

of the Liziping and Fulongchang deposits yielded mineralization ages of around 27–30 Ma (Wang et al., 2015; Zou et al., 2015, reference therein).

### 2.2. Shangnuluo deposit

The deposit is located in the Weixi County, with local exposed sequences being mainly Quaternary sandy-pebbly and clayey beds, Jurassic Huakaizuo Fm. (upper member) ($J_2h^2$) silty slate (interbedded with quartz sandstone and dolomitic limestone), Huakaizuo Fm. (lower member) ($J_2h^1$) sericite slate (interbedded with calcareous slate and quartz sandstone), Upper Permian ($P_2a$) phyllite and conglomerate, and Lower Permian ($P_1$) slate-limestone interbeds. Major local structure is the Pingzi inverted complex anticline, which developed other NW-trending structures, interlayer faults and shear zones, among which fault $F_5$ is closely ore-related. Magmatic rocks crop out in the northern, western, southern and northwestern Shangnuluo as stocks and dykes (Fig. 1c).

Orebodies at Shangnuluo are mainly hosted in the Lower Permian sericite slate and its interlayer faults (as quartz veins). The contact between orebodies and wall-rocks are sharp. Well crystallized pyrite aggregates (size: 1–3 mm) are commonly found in the hanging wall/footwall slate. Ores appear as disseminations, veinlets, massive or bands (Fig. S1i–l). Metallic minerals include mainly sphalerite, galena, boulangerite, jamesonite and pyrite, and minor boumonite, arsenopyrite, Sb tetrahedrite and chalcopyrite. Non-metallic minerals are dominated by quartz. In hand specimens and under the microscope, boulangerite coexists with greyish boulangerite and crosscuts arsenopyrite, whilst euhedral pyrite is included inside sphalerite. Meanwhile, sphalerite is included in galena and boulangerite, and boulangerite occurs as sphalerite fracture infill. This indicates a paragenetic sequence (from youngest to oldest) of pyrite, sphalerite, galena (arsenopyrite), boulangerite, and jamesonite (Fig. 2g–i).

### 2.3. Sampling

A total of 68 ore samples, 24 from Liziping, 10 from Fulongchang and 34 from Shangnuluo, were collected in this study. A detailed description of the samples can be found in Table S1. In the laboratory, some samples were cut into thin section for microscope and Raman analysis (see details in Section 3). Other samples were crushed, and sulfide minerals were separated by hand-picking under a binocular microscope, and about 2 g of each sulfide separate was picked and manually crushed into 200 mesh in an agate mortar prior to chemical analysis (see details in Section 4).

## 3. Fluid inclusions from Shangnuluo Pb-Zn ores

### 3.1. Petrographic features

Hydrothermal quartz at Shangnuluo contains numerous primary fluid inclusions (FIs). These FIs are mainly ellipsoidal or negative crystal shape, and minor elongated irregularly-shaped. According to the FI occurrences under room temperature, including their vapor-liquid ratio, phase and compositions, these primary FIs can be divided into: (1) aqueous (A)-type ($H_2O$ mainly, minor gas phase), (2) vapor-phase (B)-type (vapor-liquid ratio > 50%), (3) $CO_2$-$H_2O$ three-phase (C)-type (including $CO_2$-/$H_2O$-rich phase) (Fig. 3a–f).

A-type FIs account for ~10% of the total FIs. These FIs are 2.0–30.5 μm (mostly < 10 μm and minor 15–30 μm) in diameter, and are ellipsoidal, scattered, irregularly-shaped and minor negative crystal shape. Under room temperature, A-type FIs are vapor-liquid two-phase, with the vapor-liquid ratios of 5–20% (average ~ 10%) (Fig. 3a–c).

B-type FIs account for ~20% of the total FIs. These FIs comprise either pure $CO_2$ or $CO_2$-$H_2O$ two-phase, with sizes of 5–10 μm. B-type FIs appear mainly as negative crystal shape and ellipsoidal, and minor as irregularly-shaped (Fig. 3a–f).

C-type FIs account for ~70% of the total FIs. These FIs are 3.0–28 μm (mostly 8–12 μm) in diameter, and appear mainly as ellipsoidal or negative crystal shape, and minor irregularly-shaped. Volume proportion of $CO_2$ ($L_{CO2}$ + $V_{CO2}$) varies widely in C-type FIs, and these FIs can be further divided into $CO_2$-rich and $H_2O$-rich three-phase subtypes (Fig. 3b–d, f).

### 3.2. Fluid inclusion microthermometric data and related parameters

For C-type FIs, the melting temperatures of solid $CO_2$ are of −59.0 to −56.6 °C, slightly lower than the triple-point temperature (−56.6 °C) of pure $CO_2$, which indicates the presence of other gas phases. Raman analysis indicates that these minor gas phases may have

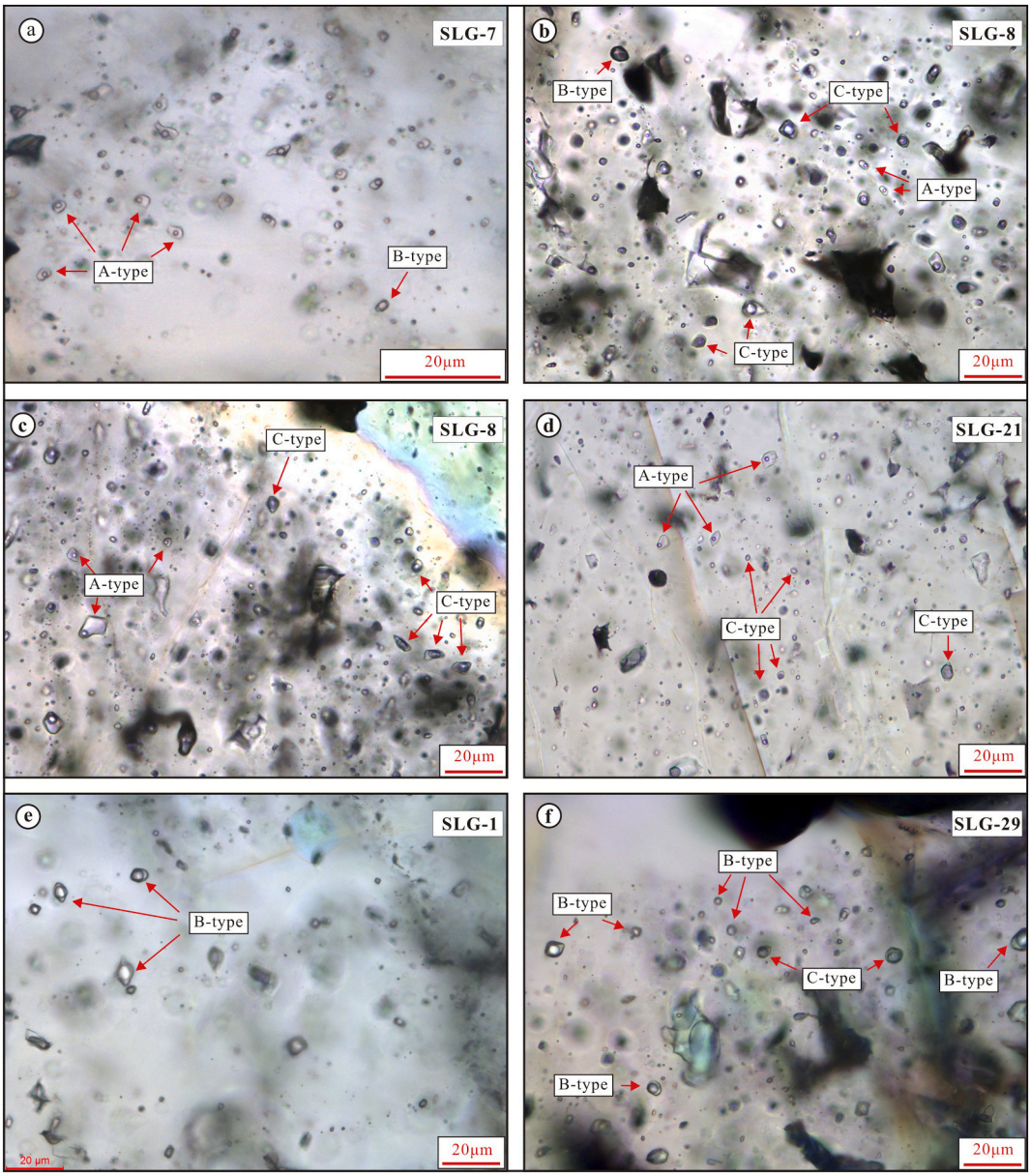


**Fig. 3.** Microphotographs of fluid inclusions (FI) from quartz in the Shangnuluo quartz vein-type Pb-Zn ores, showing coexistence of different FI types. A-type FI: Aqueous ($H_2O$) dominant, vapor-liquid ratios < 20%; B-type FI: Vapor dominant, vapor-liquid ratios > 50%; C-type FI: three-phases (vapor $CO_2$, liquid $CO_2$ and $H_2O$) (see text for details).

been $N_2$ and $CH_4$. Melting of $CO_2$ clathrate occurred at 8.2–9.4 °C, corresponding to salinity of 3.57–1.23 wt% NaCl eqv. (Roedder, 1984). Vapor-phase $CO_2$ homogenized partially (to liquid phase) at 11.5–29.7 °C, and completely at 250–310 °C (peak at 270–290 °C) (n = 225).

The degree of filling of $CO_2$-phase in the C-type FIs ranges widely. The $CO_2$-phase would generally shrink with heating in the $H_2O$-rich $H_2O$-$CO_2$-type FIs, and eventually homogenized to the $H_2O$-phase, and the opposite occurred in the $CO_2$-rich C-type FIs (with $H_2O$-phase being homogenized into $CO_2$-phase). Both $CO_2$-rich and $H_2O$-rich C-type FIs have similar homogenization temperature and pressure (100–200 MPa, average 176 MPa) (calculated with the equation proposed by Bowers and Helgeson (1983)), suggesting that they were fluid inclusion assemblage trapped coevally during $CO_2$-low-salinity fluid immiscibility (Lu et al., 2004).

The large A-type FIs (n = 5) have freezing temperature of −6.7 to −2.9 °C, corresponding to salinity of 4.80–10.1 wt% NaCl eqv. (Bodnar, 1993). The vapor phase of these FIs homogenized to liquid phase at 119.5–139.5 °C.

Our FI study indicates that the Shangnuluo Pb-Zn ore-forming fluids belong to a low-salinity NaCl-$H_2O$-$CO_2$ system. Fluid immiscibility may have occurred in the early stage of the ore-fluid evolution, which generated a $CO_2$-rich and a $H_2O$-$CO_2$ component. With the decreasing hydrothermal temperature, the fluids evolved toward a NaCl-$H_2O$ system.

## 4. Methods

### 4.1. Sulfur isotope analysis

The analysis was conducted at the Key Laboratory of Ore Deposit Geochemistry, Institute of Geochemistry, Chinese Academy of Sciences (IGCAS), using a Thermo Scientific MAT 253 (ThermoFinnigan) coupled with Flash EA 2000 element analyzer in combination with a Conflo IV continuous flow preparation device, following a previous method (Studley et al., 2002). Briefly, the sulfide/sulfosalt mineral sample powders were first weighted, wrapped inside a tin-foil cup, and then flash-combusted (at 1020 °C) in a single reactor filled with $WO_3$ and Cu as reducing agents, liberating $SO_2$ during interaction with an $O_2$-enriched He gas. The generated $SO_2$ was carried into the mass spectrometer (in a helium carrier gas) for the $\delta^{34}S$ analysis. The international sulfur isotope standard V-CDT was used in the analysis, and the standard IAEA-S-1 ($\delta^{34}S_{V\text{-}CDT}$ = −0.3‰), IAEA-S-2 ($\delta^{34}S_{V\text{-}CDT}$ = 22.6‰) and IAEA-S-3 ($\delta^{34}S_{V\text{-}CDT}$ = −32.5‰) was analyzed to monitor the analytical quality, yielding relative analytical error of < ± 0.1‰ (2σ).

### 4.2. Total Hg content and Hg isotope analyses

Total Hg (THg) concentration and Hg isotopic composition were measured at IGCAS. About 100 mg of samples were weighted in Teflon tubes, and were digested with 5 mL aqua regia ($HCl/HNO_3$ = 3/1, v/v) under 95 °C for 12 h. THg concentration of the digests were measured by a F-732 Cold Atomic Adsorption Mercury Analyzer (F-732, Shanghai Huaguang Instrument), following a previous method by Yin et al. (2013). The detection limit of F-732 analyzer is 0.05 μg/L Hg. Standard reference GSS-5 (soil) was included in the THg analysis, which yielded THg recoveries of 90–110% (n = 3). Analysis of sample duplicates showed uncertainty of < 10%.

Based on the THg measured above, the sample digests were diluted to 1 ng/mL with 10% HCl (v/v) before Hg isotope analysis using a Neptune Plus Multicollector-Inductively Coupled Plasma Mass Spectrometer (MC-ICP-MS). Details about the instrumentation and operating conditions have been reported by Yin et al. (2016). Instrumental mass bias was corrected by the standard sample bracket (SSB) method. The bracketing NIST-3133 Hg standard solutions were prepared in the same way as the samples. THg and acid matrices were matched well between sample digest and its bracketing NIST-3133 Hg standard. MDF is expressed in $\delta^{202}Hg$ notation in units of ‰ referenced to the NIST-3133 Hg standard (analyzed before and after each sample):

$$\delta^{202}Hg(‰) = [(^{202}Hg/\ ^{198}Hg_{sample})/(^{202}Hg/\ ^{198}Hg_{standard}) - 1] \times 1000 \quad (1)$$

MIF is reported in Δ notation, which describes the difference between the measured $\delta^{xxx}Hg$ and the theoretically predicted $\delta^{xxx}Hg$ value, in units of ‰:

$$\Delta^{xxx}Hg \approx \delta^{xxx}Hg - \delta^{202}Hg \times \beta \quad (2)$$

β is equal to 0.2520 for $^{199}Hg$, 0.5024 for $^{200}Hg$, and 0.7520 for $^{201}Hg$. NIST-3177 standard solutions (the commercial version of UM Almadén standard solution), were diluted to 1 ng/mL Hg in 10% HCl (v/v) and measured in every 10 samples to monitor the data quality. Analytical uncertainty was estimated based on replication of the NIST-3177 standard solution. Our results on NIST-3177 ($\delta^{202}Hg$ = −0.50 ± 0.07‰, $\Delta^{199}Hg$ = 0.02 ± 0.10‰, $\Delta^{200}Hg$ = 0.01 ± 0.08‰, and $\Delta^{201}Hg$ = −0.02 ± 0.10‰, 2SD, n = 10) are consistent with the recommendation values (Bergquist and Blum, 2007).

### 4.3. LA-ICP-MS sphalerite and sphalerite fluid inclusion analysis

Major (S, Zn, Fe, Mn) and trace element (Cd, Hg) analyses of representative samples were conducted with LA-ICP-MS at IGCAS, following a method by Lan et al. (2018). The analysis was performed with an ASI RESOLution-LR-S155 laser microprobe equipped with a Coherent Compex-Pro 193 nm ArF excimer laser, coupled with an Agilent 7700× ICP-MS instrument. Helium (350 mL/min) and Ar (900 mL/min) were used as carrier or transport gas, respectively. Each analysis incorporated a background acquisition of approximately 30 s (gas blank) followed by 60 s of data acquisition from the sample. Analyses were run with 26 μm spot size, 5 Hz pulse frequency and 3 J/cm$^2$ fluence. For FI analysis, we chose some vapor-dominant FIs inside sphalerite from Shangnuluo (Fig. S2). The FI components were analyzed with the aforementioned procedures, but the Mg, K and Ca (which are high in FIs) were also simultaneously measured. Once the FIs was opened, the synchronously peaks of Mg, K, Ca and other target elements (e.g., Hg) would appear in the single-spot LA-ICP-MS spectra (Cook et al., 2009) of sphalerite. These Hg analyses (without standard) can provide an estimation of Hg concentration in FIs, based on the Hg signal intensity comparison between the sphalerite and its FIs, if the sphalerite Hg concentration has been determined by other methods (e.g., MC-ICP-MS).

## 5. Results

### 5.1. THg content and Hg-S isotopes of quartz vein-type Pb-Zn-Sb deposit

For the Shangnuluo ore sulfides, the THg contents are 30.7–365 μg/g (average 115 μg/g, n = 22) for the sphalerite, 0.92–5.79 μg/g (average 2.46 μg/g, n = 3) for the pyrite, 0.40–1.01 μg/g (average 0.70 μg/g, n = 4) for the galena, and 0.10–6.68 μg/g (average 2.88 μg/g, n = 5) for the boulangerite (Table S1).

As for sulfide $\delta^{202}Hg$, the analyses yielded 0.32–2.71‰ (average 2.09 ± 1.10‰, 2SD, n = 22) for the sphalerite, 1.62–2.38‰ (average 1.96 ± 0.78‰, 2SD, n = 3) for the pyrite, 1.22–2.05‰ (average 1.71 ± 0.74‰, 2SD, n = 4) for the galena, and −0.40–0.80‰ (average 0.23 ± 1.04‰, 2SD, n = 5) for the boulangerite (Table S1). The average $\delta^{202}Hg$ values of the Shangnuluo sulfides follow the following sequence: $\delta^{202}Hg_{Sp} > \delta^{202}Hg_{Py} > \delta^{202}Hg_{Gn} > \delta^{202}Hg_{Blr}$. Compared to the published $\delta^{202}Hg$ values of sphalerite (e.g., Sonke et al., 2010; Yin et al., 2016; Tang et al., 2017; Xu et al., 2018) or seafloor hydrothermal vent sulfides ($\delta^{202}Hg$: −0.37 to −0.01‰,

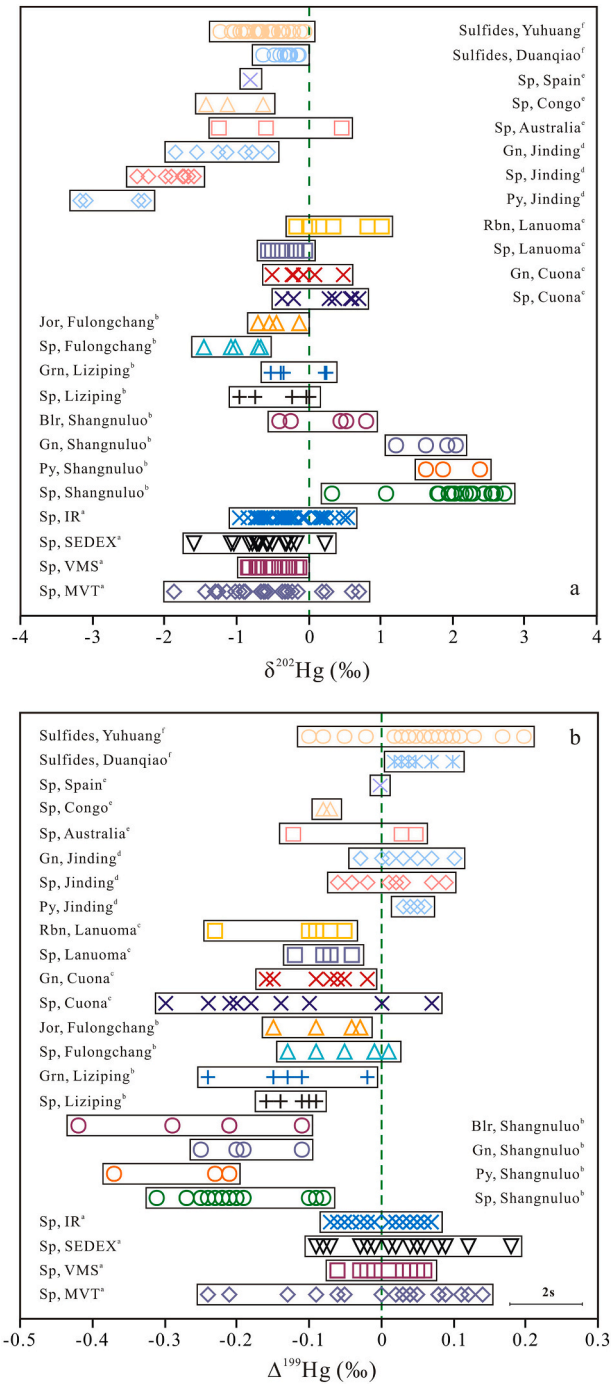


**Fig. 4.** Comparison of Hg isotope compositions between different ore sulfides from various Pb-Zn deposits in the region: (a) $\delta^{202}$Hg; (b) $\Delta^{199}$Hg. Abbreviations: Sp-sphalerite, Py-pyrite, Gn-galena, Jor-jordanite, Grn-gratonite, Blr-boulangerite, Rbn-robinsonite. Data source: [a]Sedimentary exhalative deposits (SEDEX), Mississippi Valley type (MVT), volcanic hosted massive sulfides (VMS) and intrusion related deposits (IR), Yin et al. (2016); [b]this study; [c]Xu et al. (2018); [d]Tang et al. (2017); [e]Sonke et al. (2010); [F]sulfides from Duanqiao and Yuhuang hydrothermal fields in the Southwest Indian Ridge (Zhu et al., 2020).

n = 3; Sherman et al., 2009; $\delta^{202}$Hg: −1.23 to −0.05‰, Zhu et al., 2020), the Shangnuluo ore sulfides (sphalerite, pyrite and galena) contain distinctly positive $\delta^{202}$Hg (up to 2.71‰; Fig. 4a).

In general, the Shangnuluo sulfide/sulfosalt minerals show negative $\Delta^{199}$Hg values, i.e., −0.31 to −0.08‰ (average −0.21 ± 0.12‰, 2SD, n = 15) for the sphalerite; −0.37 to −0.21‰ (average −0.27 ± 0.17‰, 2SD, n = 3) for the pyrite, −0.25 to −0.11‰ (average −0.19 ± 0.12‰, 2SD, n = 4) for the galena, and −0.42 to −0.11‰ (average −0.25 ± 0.23‰, 2SD, n = 4) for the boulangerite.

The Lower Permian sericite slate and limestone ore hosts at Shangnuluo contain very similar total Hg content (12.2 to 25.5 ng/g), relatively uniform $\delta^{202}$Hg (−0.90 to 0.23‰) and insignificant Hg-MIF ($\Delta^{199}$Hg: −0.08 to 0.08‰) (Table S2), resembling those of the regional metamorphic basement rocks ($\Delta^{199}$Hg: −0.19 to −0.08‰; according to Xu et al. (2018)).

The Shangnuluo sulfide/sulfosalt minerals contain relatively light S isotope ($\delta^{34}$S) compositions, i.e., −5.2 to −4.4‰ (average −4.7 ± 0.2‰, 2SD, n = 3) for pyrite, −13.0 to −2.7‰ (average −5.6 ± 5.5‰, 2SD, n = 3) for sphalerite, −11.1 to −8.3‰ (average −8.9 ± 1.2‰, 2SD, n = 4) for galena, and −10.6 to −9.0‰ (average −9.5 ± 1.5‰, 2SD, n = 4) for boulangerite/jamesonite, similar to those of the pyrite aggregates in the ore-hosting slate ($\delta^{34}$S: −13.0‰ and −6.1‰) (Table S3).

### 5.2. THg content and Hg-S isotopes of MVT Pb-Zn deposits

Sulfide/sulfosalt THg contents of the Liziping and Fulongchang Pb-Zn deposits are in general higher than those of the Shangnuluo deposit. For the Liziping deposit, our analysis yielded 285–3853 μg/g (average 1798 μg/g, n = 5) for the sphalerite, and 14.0–289 μg/g (average 78.2 μg/g, n = 5) for the gratonite. For the Fulongchang deposit, our analysis yielded 215–2603 μg/g (average 1072 μg/g, n = 6) for the sphalerite, and 65.4–179 μg/g (average 103 μg/g, n = 4) for the jordanite (Table S1).

Sulfide $\delta^{202}$Hg values of the Liziping and Fulongchang deposits range −0.95 to 0.25‰ (average −0.27 ± 0.79‰, 2SD, n = 10) and −1.46 to −0.13‰ (average −0.82 ± 0.86‰, 2SD, n = 10), respectively. Such ranges are similar to those of the published Pb-Zn ore sulfides (−1.41 to 0.46‰; Sonke et al., 2010), and those of the sphalerite from major Pb-Zn deposits in China (−1.87 to 0.70‰; Yin et al., 2016), Cuona galena and sphalerite (−0.50 to 0.61‰, n = 17; Xu et al., 2018), and Lanuoma Pb-Zn sulfides (−0.57 to 1.01‰, n = 14; Xu et al., 2018), but generally higher ($p < 0.05$, *t*-test) than those from the Jinding Pb-Zn deposit (−3.17 to −0.57‰, n = 22; Tang et al., 2017).

Compared with the early-stage sphalerite from Liziping and Fulongchang, the late-stage gratonite/jordanite from the same deposits have generally higher $\delta^{202}$Hg ($p < 0.05$, t-test), cf. early-stage sphalerite (Liziping: −0.95 to 0.00‰, average −0.39 ± 0.87‰, 2SD, n = 5; Fulongchang: −1.46 to −0.66‰, average −1.06 ± 0.69‰, 2SD, n = 6) and late-stage gratonite (Liziping: −0.52 to 0.25‰, average −0.16 ± 0.73‰, 2SD, n = 5) and jordanite (Fulongchang: −0.71 to −0.13‰, average −0.46 ± 0.49‰, 2SD, n = 4). Sulfides/sulfosalts from both Liziping and Fulongchang showed slightly negative to near-zero $\Delta^{199}$Hg values, ranging from −0.24 to −0.02‰ (average −0.13 ± 0.12‰, 2SD, n = 10) and −0.15 to 0.01‰ (average −0.06 ± 0.10‰, 2SD, n = 10), respectively.

$\delta^{34}$S values of the sphalerite, gratonite and anhydrite from Liziping are of 5.5–8.7‰ (average 6.2 ± 1.4‰, 2SD, n = 5), 5.8–6.8‰ (average 6.4 ± 0.8‰, 2SD, n = 5), and 14.2–16.2‰ (average 15.5 ± 1.4‰, 2SD, n = 15), respectively, whilst those of the sphalerite and jordanite from Fulongchang are of 6.8–8.5‰ (average 7.5 ± 1.3‰, 2SD, n = 5) and 4.3–6.5‰ (average 5.7 ± 1.9‰, 2SD, n = 4), respectively. These results are consistent with those reported in the region ($\delta^{34}$S: 2.4–10.5‰; Wang et al., 2015).

### 5.3. Intra-grain THg distribution in sphalerite and fluid inclusions

Although the sphalerite THg contents of the basinal brine-related Liziping and Fulongchang deposits are 1–2 order of magnitude higher than those of the quartz-vein-type Shangnuluo deposit, LA-ICP-MS Hg spectra of the sphalerite from both deposit types are featured by being

flat (Fig. 6a–d), indicating that Hg exist as solid solution in the sphalerite sample. For the sphalerite (sample SLG-28) from Shangnuluo, LA-ICP-MS analysis of the two vapor-rich FIs (Spots 3 and 6; Fig. 6e–f) indicate that their $^{202}$Hg signal counts are 1.4–4.1 times higher ($p < 0.05$, *t*-test) than those of the sphalerite (average 30–80/s) (dependent on FI size), suggesting the presence of Hg-rich vapor phase in the ore-forming fluids.

## 6. Discussion

### 6.1. THg variation in different ore sulfides

Sulfide THg variations of different deposit types are controlled by the following factors: (1) Ore fluid nature: Mercury contents are higher in relatively oxidizing and alkaline fluids (Varekamp and Buseck, 1984; Fein and Williams-Jones, 1997; Smith et al., 2008); (2) variation in Hg background concentration: Yin et al. (2012) considered that the high Hg background in sedimentary rocks may have led to the relatively high sphalerite Hg contents in MVT and SEDEX deposits; (3) mode of Hg occurrence in sulfides: Mercury commonly occurs as Hg(II) to replace Zn(II) in the sphalerite crystal lattice (Grammatikopoulos et al., 2006; Cook et al., 2009). Anomalously high sphalerite Hg contents may have been related to solid solution or micro-inclusions of Hg minerals, such as cinnabar (HgS), coloradoite (HgTe), tiemannite (HgSe) (George et al., 2016); (4) extent of closure of ore formation system and process: Mercury is a volatile element, and readily enters the vapor phase and migrates toward the ground surface. Fluid boiling would have generated massive Hg vaporization, leading to Hg depletions in the residual fluids (e.g., Smith et al., 2005, 2008).

Comparisons of geological and geochemical features, sulfide THg contents, and Hg-S isotopic compositions of typical Pb-Zn deposits in the STMB are listed in Table S4. Ore-forming fluids of the Jinding, Liziping, Fulongchang deposits were all likely sourced from basinal brine, therefore, the difference of THg contents between those deposits is not controlled by ore-forming fluid nature. It is commonly considered that these Pb-Zn deposits were formed in the large-scale Himalayan nappe system after the India-Asia collision (Hou et al., 2007; He et al., 2009; Deng et al., 2014; Bi et al., 2019). We notice that consistently low THg contents (12.2–150 ng/g) are present in the metamorphic basement and sedimentary rocks in the Lanping and Changdu basins (Table 2; Xu, 2017), similar to the sedimentary/magmatic/metamorphic rocks in the California Coast Ranges (16.5–288 ng/g; Smith et al., 2008) (Fig. S3). Therefore, the dramatic difference ($p < 0.05$, t-test) in sulfides between the Liziping (14.0–3853 μg/g), Fulongchang (35.4–2603 μg/g), Shangnuluo (0.40–365 μg/g) and Jinding (0.472–1.01 μg/g; Tang et al., 2017) deposits are unlikely caused by basement Hg background concentrations. As no Hg-rich minerals or inclusions were found in the sphalerite from these deposits (Figs. 2 and 6a–d), difference in modes of Hg occurrence in sulfides can be ruled out.

By excluding the above-mentioned factors, we hypothesized that the variation of sphalerite THg in these deposits may have been influenced by ore-forming processes. Considering Hg is highly volatile and readily lost from ore-forming fluids in an open hydrothermal system, it is likely that the sphalerite THg contents can be indicative of the degree of closure of ore formation systems. For instance, the coarse-grained texture of the Liziping and Fulongchang sulfide ores, the lack of evidence for ore-forming fluid boiling (Wang et al., 2015), and the relatively higher sphalerite THg contents, all suggest that these sulfides were formed in less open environment with limited Hg loss from the ore-forming fluids. In contrast, the generally fine-grained or disseminated ore textures, the extremely low sphalerite THg contents (< 1.01 ppm, Tang et al., 2017; Table S4), and the fluid boiling effect (Xue et al., 2007) at Jinding all indicate that the sulfide ores were precipitated rapidly in a relatively open environment, and Hg may have already escaped from the fluids before sulfide precipitation. The presence of Hg-rich vapor phase in FIs from the Shangnuluo deposit (Fig. 6e–f and S2) suggests that ore-forming fluids were separated into two phases (the Hg-rich vapor phase and the Hg-poor liquid phase).

### 6.2. Sulfide mass-dependent fractionation of Hg isotopes

Previous field and experimental studies suggested that distinct MDF occurs during the following processes: (1) $Hg^0$ evaporation and volatilization: e.g., aqueous $Hg^0$ volatilization (Zheng et al., 2007), dynamic $Hg^0$ liquid-vapor-phase vaporization (Estrade et al., 2009; Fig. 7a–b), and hydrothermal degassing of $Hg^0$ (Sherman et al., 2009; Fig. 7c); (2) redox reactions of mercury: e.g., aqueous $Hg^{II}$ dark reduction (Zheng and Hintelmann, 2009), aqueous $Hg^{II}$ photoreduction (Bergquist and Blum, 2007), aqueous $Hg^{II}$ microbial reduction (Kritee et al., 2007; Fig. 7d), gaseous $Hg^0$ photo-oxidation (Sun et al., 2016), and oxidative condensation of $Hg^0_{g(gas)}$ (Zambardi et al., 2009; Fig. 7e); (3) precipitation of Hg-bearing minerals, e.g., meta-cinnabar (*β*-HgS) (Smith et al., 2015, Fig. 7f). These physicochemical processes were generally involved the mobilization, transport and precipitation of Hg during the formation of deposit.

Smith et al. (2008) suggested that limited Hg-MDF (below ± 0.5‰ in $\delta^{202}$Hg) should occur during the Hg mobilization from source rocks. Previous studies reported large $\delta^{202}$Hg variations (up to 5‰) in epithermal Hg deposits, which were interpreted to be related to $Hg^0$ evaporation during the fluid boiling (Smith et al., 2005, 2008). For Pb-Zn deposits, the mixing between an oxidizing metal-rich (e.g., Zn, Pb, Hg) fluid and a reducing sulfur-rich fluid is commonly used to account for the Pb-Zn ore precipitation (Leach et al., 2005; Xue et al., 2007; He et al., 2009; Tang et al., 2017; Bi et al., 2019). Under most circumstances, Hg in the ore-fluids comprise $Hg^0_{aq}$ or $Hg^0_{vapor}$ species (Varekamp and Buseck, 1984). When metal sulfides (e.g., (meta)-cinnabar, sphalerite) precipitate (Smith et al., 2008), the fluid $Hg^0$ has to be oxidized to $Hg^{II}$ to enter the sulfide/sulfosalt crystal lattice. As sulfides are formed in reducing environment, the oxidation of $Hg^0$ would likely occur during the fluid migration (instead of during sulfide precipitation). For deep-seated ore sulfides, their Hg isotope compositions would depend on the proportion of $Hg^0$ (to THg) that had vaporized.

Previous studies indicated that boiling and separation of Hg-bearing $CO_2$-phase would lead to significant fluid Hg isotopic changes (Smith et al., 2008). We hypothesized that $Hg^0$ evaporation during the fluid boiling was important in causing the $\delta^{202}$Hg variation of our samples. We observed much wide $\delta^{202}$Hg ranges at Shangnuluo (−0.40 to 2.71‰), which is consistent with the FI evidence of fluid immiscibility, and support the occurrence of fluid boiling (Fig. 3). In the Liziping and Fulongchang deposits, where boiling was likely limited (Wang et al., 2015), a narrow $\delta^{202}$Hg range (−1.46 to 0.25‰) was observed. Compared with the early-stage sphalerite and pyrite, late-stage sulfides (gratonite, jordanite, galena) from Liziping, Fulongchang, Lanuoma and Jinding have generally heavier $\delta^{202}$Hg (Fig. 4a). As fluid boiling was not commonly observed in these deposits, the lower $\delta^{202}$Hg in the early-stage sulfides may be explained by preferentially precipitation of lighter Hg isotopes in the sulfides, as suggested by Smith et al. (2015). At Shangnuluo, the lowest $\delta^{202}$Hg was observed in the late-stage boulangerite, which was formed due to oxidization of condensed $Hg^0$. For the Shangnuluo sphalerite, negative correlation occurs between $\delta^{202}$Hg and THg content ($R^2 = 0.765$, $p < 0.01$) (Fig. 5a), indicating that the Shangnuluo mineralization may have experienced a mixed Hg from the vapor phase (low $\delta^{202}$Hg, high THg) and residual aqueous phase (high $\delta^{202}$Hg, low THg).

### 6.3. Sulfide mass-independent fractionation of Hg isotopes

Hg-MIF is thought to be caused by nuclear volume effect (NVE) and magnetic isotope effect (MIE) (Schauble, 2007; Zheng and Hintelmann, 2009; Sonke, 2011; Ghosh et al., 2013; Motta et al., 2020). NVE occurs during several processes such as elemental $Hg^0$ evaporation (Estrade

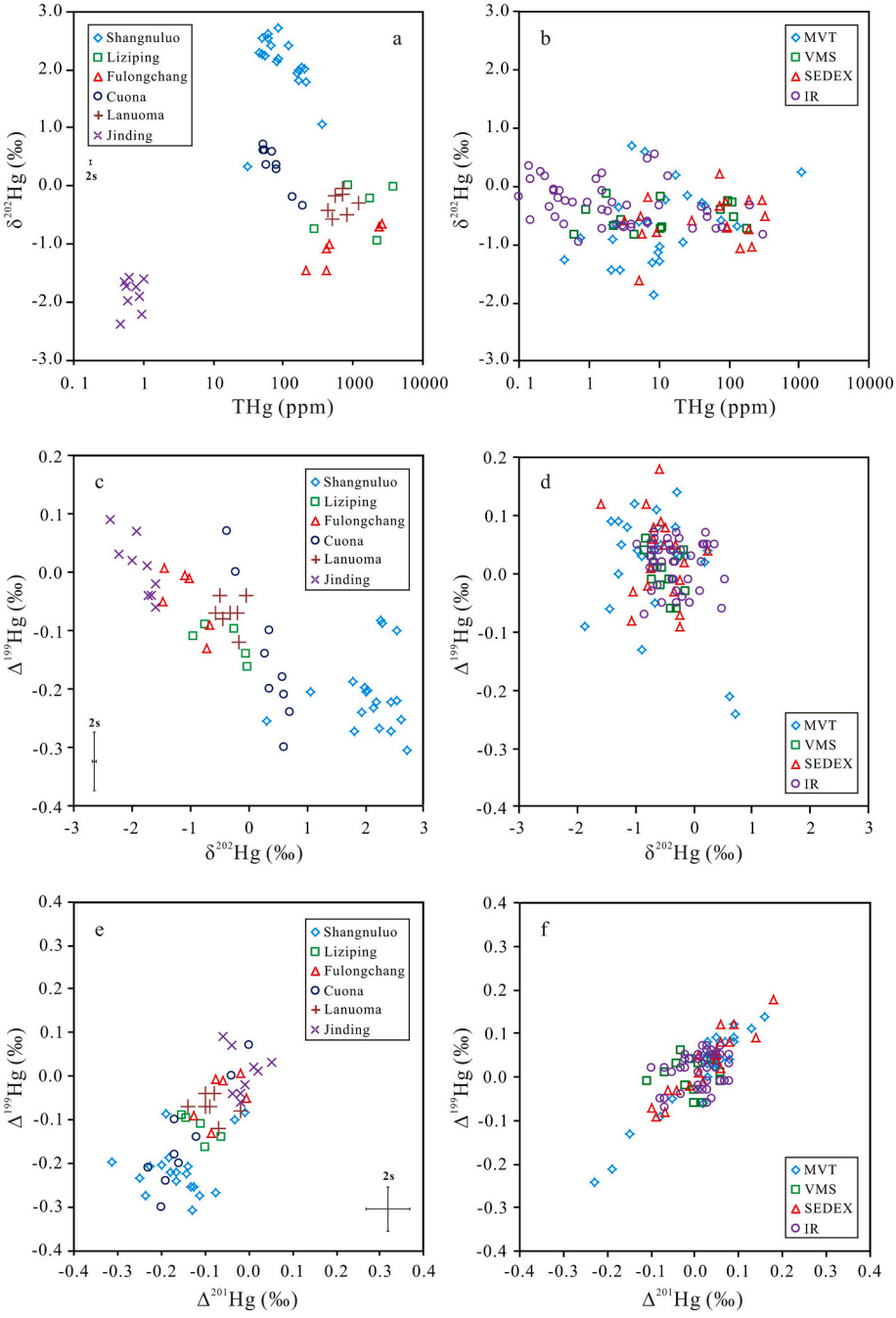


**Fig. 5.** Plots comparing the sphalerite THg contents and Hg isotopes of deposits from the Sanjiang Tethyan metallogenic belt and four major types of Pb-Zn deposits in China. Data source: Jinding deposit (Tang et al., 2017), Lanuoma and Cuona deposits (Xu et al., 2018); SEDEX, MVT, VMS and IR deposits (Yin et al., 2012, 2016).

et al., 2009; Ghosh et al., 2013) and dark $Hg^{II}$ reduction (Zheng and Hintelmann, 2010), which are associated with $\Delta^{199}Hg/\Delta^{201}Hg$ of ~1.6 to ~1.7; MIE mainly occurs during photochemical processes such as aqueous $Hg^{II}$ photoreduction and photo-degradation of MeHg, with $\Delta^{199}Hg/\Delta^{201}Hg$ ratios of 1.0 and 1.3, respectively (Bergquist and Blum, 2007; Zheng and Hintelmann, 2010; Motta et al., 2020). Large-magnitude Hg-MIF (a variation of ~10‰ in $\Delta^{199}Hg$) in natural samples (e.g., atmosphere, rain water, aquatic organisms) mainly occurs during photochemical processes in surface environments (Sonke, 2011; Blum et al., 2014).

The observed significant Hg-MIF signals in natural samples in Earth's surface reservoirs were attributed to $Hg^{II}$ photoreduction (Sonke, 2011; Blum et al., 2014). In comparison, mantle and volcanic materials have insignificant Hg-MIF signal ($\Delta^{199}Hg$ ~ 0‰, Smith et al., 2008, Sherman et al., 2009; $\Delta^{199}Hg$ 0.02–0.10‰, Zhu et al., 2020). The $\Delta^{199}Hg$ values of sulfides/sulfosalts from the Pb-Zn deposits in the STMB range from −0.42 to 0.10‰ (Table S1, Fig. 5), which are generally negative or similar to those of the basement rocks and strata samples ($\Delta^{199}Hg$ or $\Delta^{201}Hg$: generally < ± 0.2‰; Blum et al., 2014; Yin et al., 2016; Tang et al., 2017; Table S2, Fig. S3), within analytical uncertainty ( ± 0.1‰). Moreover, these sulfides/sulfosalts have $\Delta^{199}Hg/\Delta^{201}Hg$ of ~1 (Fig. 5e), which agrees well with previous results of aqueous $Hg^{II}$ photoreduction (Bergquist and Blum, 2007). Considering Hg-MIF does not occur during hydrothermal processes (Sherman et al., 2009; Zhu et al., 2020), Hg-MIF signals observed in hydrothermal deposits were explained by Hg inheritance from surface reservoirs (Sonke et al., 2010; Xu et al., 2018; Yin et al., 2016). In this regard, the negative $\Delta^{199}Hg$ signals observed in our samples may have

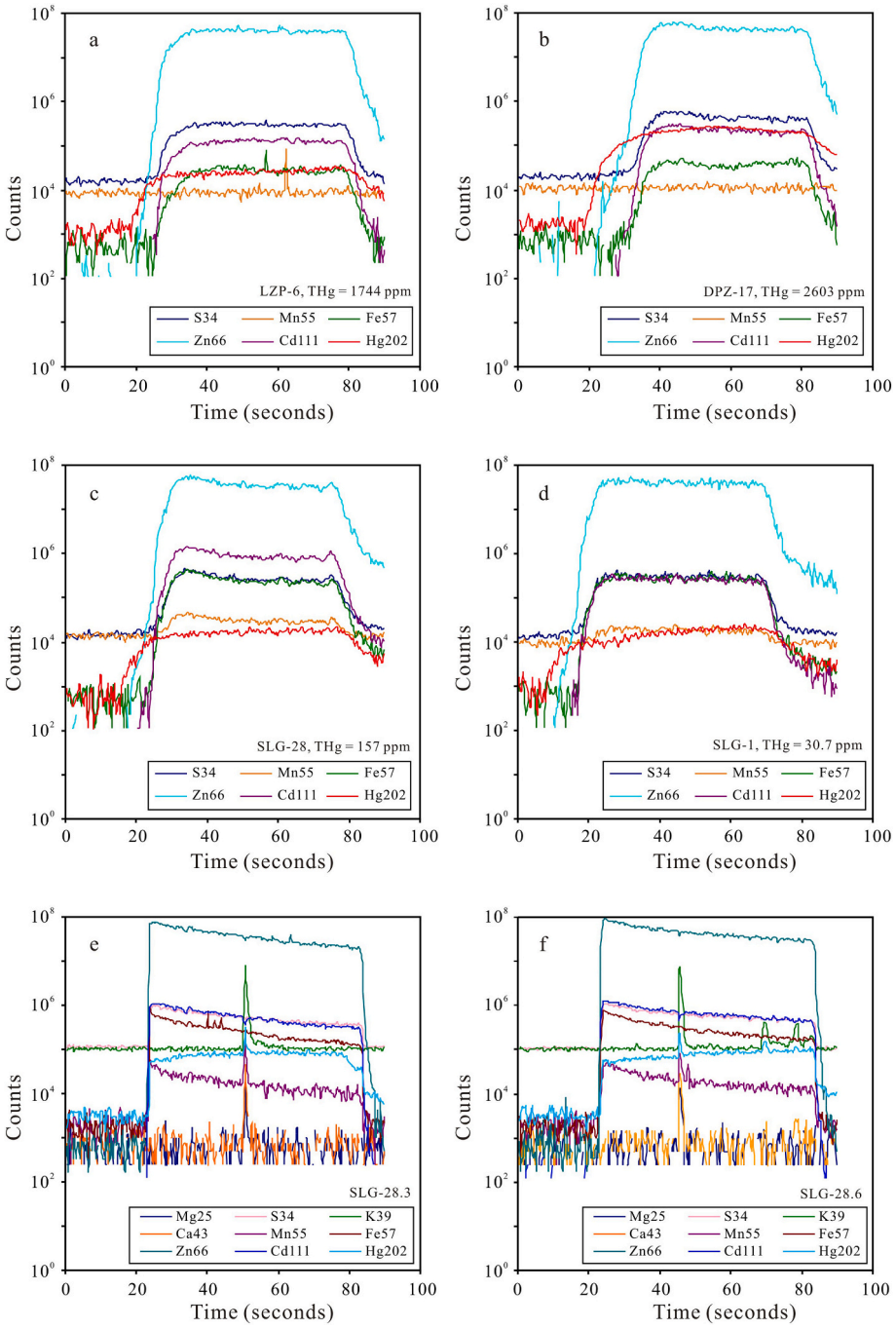


**Fig. 6.** Representative LA-ICP-MS spectra (of selected elements) for spot analyses of sphalerite from the Lanping basin (a-d). Two vapor-rich FIs in sphalerite from Shangnuluo (e-f). Significant Hg signal plateau present in the FIs (cf. sphalerite). Sample number and THg content of sphalerite of the same sample (measured by MC-ICP-MS) are also shown.

been sourced from metamorphic basement rocks, since negative $\Delta^{199}$Hg values were reported from metamorphic basement rocks in the STMB (Xu et al., 2018).

### 6.4. Discrimination of Pb-Zn deposit type via integration of Hg and S isotopes

Previous studies and our results indicate wide ranges of sulfide S isotope compositions for the different types of Pb-Zn deposits in the STMB (Table S4). These deposits have different sources of reduced sulfur in different mineralization stages. According to S isotope compositions, these deposits can be divided into four types: (1) Jinding deposit: Early-stage sphalerite and pyrite contain $\delta^{34}$S values of −48.6 to −10.2‰, whilst late-stage galena contains relatively high $\delta^{34}$S value (−8.3–7.7‰). Sulfur isotope signatures of the former and latter may have derived from bacterial sulfate reduction (BSR) and thermochemical sulfate reduction (TSR), respectively (He et al., 2009; Tang et al., 2014; Xue et al., 2015; Yalikun et al., 2018); (2) Liziping, Fulongchang and Cuona deposits: The $\delta^{34}$S values are relatively high (2.5–11.2‰), especially at Liziping and Fulongchang where sulfates (gypsum, anhydrite, barite) were found coexisting with sulfides (sulfate $\delta^{34}$S: 13.7–16.2‰), which indicate that the reduced sulfur was mainly derived from TSR processes (Wang et al., 2015; Xu, 2017; this study); (3) Shangnuluo deposit: Sulfide $\delta^{34}$S values are relatively low (−13.0

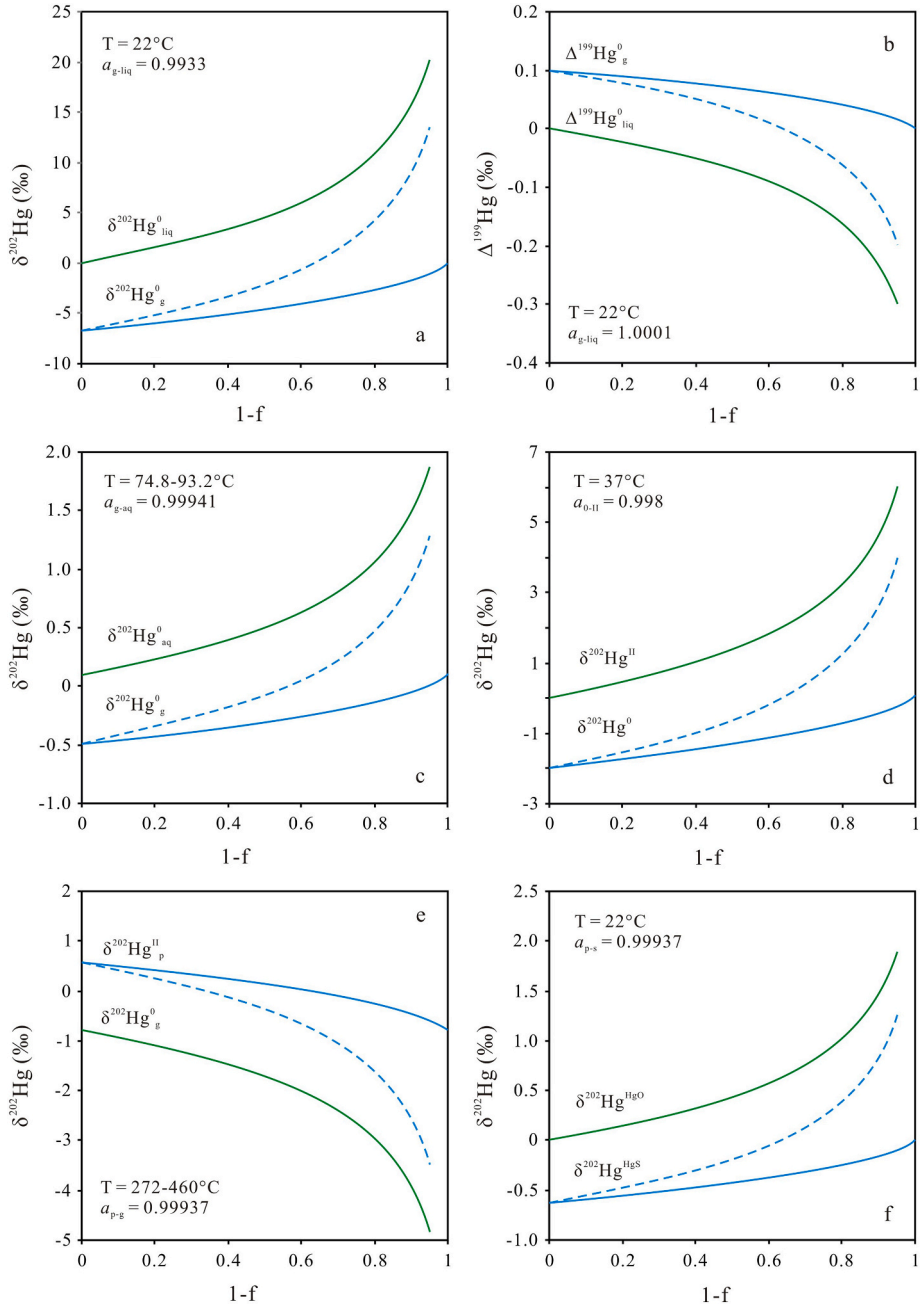


**Fig. 7.** Mercury isotopic fractionation of different geologic/geochemical processes (observed in field and experimental studies). Dynamic liquid-vapor evaporation of $Hg^0$ (a, b; Estrade et al., 2009); Degassing of hot spring water (c; Sherman et al., 2009); Reduction of Hg(II) to Hg(0) by mercury resistant microorganisms (d; Kritee et al., 2007); In-plume oxidation and condensation of fumarole $Hg^T_{(fum)}$ (e; Zambardi et al., 2009); Precipitation of metacinnabar (β-HgS) (f; Smith et al., 2015).

to −2.7‰; this study), similar to the Pb-Zn ore sulfides from eastern Baiyangping orefield ($\delta^{34}S$: −7.3–2.1‰; Feng et al., 2014 and reference therein) or the late-stage galena from Jinding ($\delta^{34}S$: −8.3–7.7‰; Tang et al., 2014). The reduced sulfur may have been mainly derived from the strata, and was related to the decomposition of organic matter and the TSR (which reduced the sulfate to produce 0–20‰ fractionation at varying degrees) (Kiyosu and Krouse, 1990; Machel et al., 1995); (4) Lanuoma deposit: Early-stage sulfides (pyrite, sphalerite, boulangerite, orpiment and galena) contain near-zero $\delta^{34}S$ values (−1.6–3.3‰; Xu, 2017 and reference therein; −3.0–2.5‰; Sheng et al., 2019), indicating a probable magmatic source (Sheng et al., 2019). In contrast, the late-stage pyrite contains high $\delta^{34}S$ values (max. 6.0‰), suggesting probable mixing with reduced sulfur derived from TSR processes (Sheng et al., 2019).

Mercury isotopic compositions of Pb-Zn ore sulfides may indirectly reflect those of the Hg-bearing ore fluids at the time of sulfide precipitation, whilst sulfur isotopes reflect the reduced sulfur source and/or formation pathway of the different types of Pb-Zn deposits. Thus, integrating Hg and S isotopic evidence can possibly reveal the different ore-forming processes. As shown in Fig. 8, in the $\delta^{34}S$ vs. $\delta^{202}Hg$ (or $\Delta^{199}Hg$) diagram, the ore sulfides of the different Pb-Zn deposit types in the STMB fall into different fields. For instance, the Jinding ore sulfides show the lowest $\delta^{34}S$ and $\delta^{202}Hg$ values, and $\Delta^{199}Hg$ of ~0‰; ore sulfides from Liziping, Fulongchang and Cuona are featured by the highest $\delta^{34}S$, intermediate $\delta^{202}Hg$, and slightly negative $\Delta^{199}Hg$ values; the Shangnuluo ore sulfides have the negative $\delta^{34}S$ and highest $\delta^{202}Hg$, and the most negative $\Delta^{199}Hg$ (low to −0.42‰) values; the Lanuoma ore sulfides are characterized by near-zero $\delta^{34}S$ and $\delta^{202}Hg$, and slightly

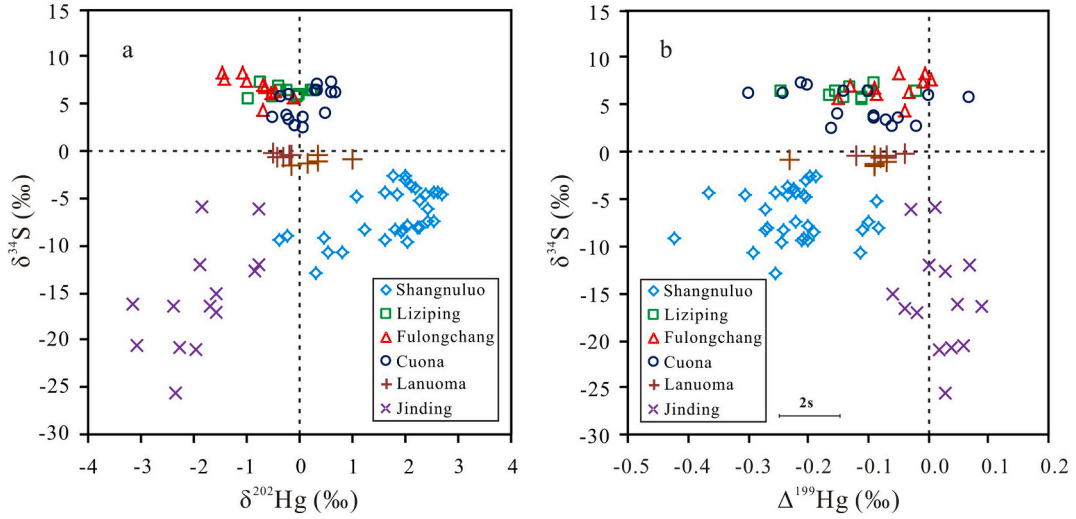


**Fig. 8.** Plots of sulfide $\delta^{34}S$ vs. Hg isotopic compositions of the different Pb-Zn deposit types in the Sanjiang Tethyan metallogenic belt. Data source: Jinding (Tang et al., 2017); Cuona and Lanuoma $\delta^{202}Hg$ and $\Delta^{199}Hg$ values (Xu et al., 2018), $\delta^{34}S$ values (Xu, 2017).

negative $\Delta^{199}Hg$ (Fig. 8a–b). Our study, therefore, demonstrated clear evidence that integration of S and Hg isotopes has good potential in discriminating different genetic types of Pb-Zn deposits.

## 7. Conclusions

For the Shangnuluo quartz vein-type Pb-Zn-Sb deposit, the ore sulfides (especially sphalerite) are featured by a large variation in $\delta^{202}Hg$, indicating $Hg^0$ evaporation from hydrothermal fluids readily occurred during the formation of this deposit. The negative $\Delta^{199}Hg$ suggests that Hg was sourced from the metamorphic basement, whereas the low $\delta^{34}S$ observed suggests that sulfur was mainly sourced from the sedimentary sequence, related to the decomposition of organic matter and the TSR. For the Liziping and Fulongchang deposits, the narrow $\delta^{202}Hg$ range suggests limited $Hg^0$ evaporation during hydrothermal mineralization. The lower $\delta^{202}Hg$ in early stage sulfides in these two deposits may be explained by preferentially precipitation of lighter Hg isotopes in sulfides. The negative $\Delta^{199}Hg$ observed in Liziping and Fulongchang again suggests Hg was derived mainly from the metamorphic basement. $\delta^{34}S$ of these two deposits also supports sulfur was sourced from sedimentary sequences, related to the TSR. This study demonstrates that combining sulfur ($\delta^{34}S$) and mercury ($\delta^{202}Hg$ and $\Delta^{199}Hg$) can provide new insights into the source and processes in the formation of Pb-Zn deposits.

Supplementary data to this article can be found online at https://doi.org/10.1016/j.chemgeo.2020.119910.

## Declaration of competing interest

The authors declare that they have no known competing financial interests or personal relationships that could have appeared to influence the work reported in this paper.

## Acknowledgments

This research was financially supported by the National Basic Research Program of China (973 Program) (2015CB452603) and National Natural Science Foundation of China (41673052, 41973047). We thank Yan-Wen Tang and Chao-Jian Qin for helping with LA-ICP-MS and Laser-Raman microspectroscopic analyses. The authors appreciate the constructive comments and suggestions of an anonymous reviewer. Language editing service by Cenozoic Editing & Consultancy (Australia) is acknowledged.

## References

Bergquist, B.A., Blum, J.D., 2007. Mass-dependent and -independent fractionation of Hg isotopes by photoreduction in aquatic systems. Science 318, 417–420.
Bi, X.W., Tang, Y.Y., Tao, Y., Wang, C.M., Xu, L.L., Qi, H.W., Lan, Q., Mu, L., 2019. Composite metallogenesis of sediment-hosted Pb-Zn-Ag-Cu base metal deposits in the Sanjiang Collisional Orogen, SW China, and its deep driving mechanisms. Acta Petrol. Sin. 35, 1341–1371 (Chinese with English abstract).
Blum, J.D., Popp, B.N., Drazen, J.C., Choy, C.A., Johnson, M.W., 2013. Methylmercury production below the mixed layer in the North Pacific Ocean. Nat. Geosci. 6, 879–884.
Blum, J.D., Sherman, L.S., Johnson, M.W., 2014. Mercury isotopes in earth and environmental sciences. Annu. Rev. Earth Pl. Sci. 42, 249–269.
Bodnar, R.J., 1993. Revised equation and table for determining the freezing point depression of $H_2O$-NaCl solutions. Geochim. Cosmochim. Acta 57, 683–684.
Bowers, T.S., Helgeson, H.C., 1983. Calculation of the thermodynamic and geochemical consequences of nonideal mixing in the system $H_2O$-$CO_2$-NaCl on phase relations in geologic systems: equation of state for $H_2O$-$CO_2$-NaCl fluids at high pressures and temperatures. Geochim. Cosmochim. Acta 47, 1247–1275.
Chen, K.X., He, L.Q., Wei, J.Q., Yang, A.P., Yang, W.G., Huang, H.L., 2004. Preliminary study on the characteristics of ore minerals and the occurrence states of sliver and cobalt in the Baiyangping ore-concentrated field, Yunnan province. Acta Mineral. Sin. 24, 61–67 (in Chinese with English abstract).
Chen, J.B., Hintelmann, H., Feng, X.B., Dimock, B., 2012. Unusual fractionation of both odd and even mercury isotopes in precipitation from Peterborough, ON, Canada. Geochim. Cosmochim. Acta 90, 33–46.
Chen, J.B., Hintelmann, H., Zheng, W., Feng, X.B., Cai, H.M., Wang, Z.H., Yuan, S.L., Wang, Z.W., 2016. Isotopic evidence for distinct sources of mercury in lake waters and sediments. Chem. Geol. 426, 33–44.
Cook, N.J., Ciobanu, C.L., Pring, A., Skinner, W., Shimizu, M., Danyushevsky, L., Saini-Eidukat, B., Melcher, F., 2009. Trace and minor elements in sphalerite: a LA-ICPMS study. Geochim. Cosmochim. Acta 73, 4761–4791.
Deng, J., Wang, Q.F., Li, G.J., Santosh, M., 2014. Cenozoic tectono-magmatic and metallogenic processes in the Sanjiang region, southwestern China. Earth-Sci. Rev. 138, 268–299.
Estrade, N., Carignan, J., Sonke, J.E., Donard, O.F.X., 2009. Mercury isotope fractionation during liquid–vapor evaporation experiments. Geochim. Cosmochim. Acta 73, 2693–2711.
Estrade, N., Carignan, J., Donard, O.F.X., 2010. Isotope tracing of atmospheric mercury sources in an urban area of Northeastern France. Environ. Sci. Technol. 44, 6062–6067.
Fein, J.B., Williams-Jones, A.E., 1997. The role of mercury-organic interactions in the hydrothermal transport of mercury. Econ. Geol. 92, 20–28.
Feng, X.B., Foucher, D., Hintelmann, H., Yan, H.Y., He, T.R., Qiu, G.L., 2010. Tracing mercury contamination sources in sediments using mercury isotope compositions. Environ. Sci. Technol. 44, 3363–3368.
Feng, C.X., Bi, X.W., Liu, S., Hu, R.Z., 2014. Fluid inclusion, rare earth element geochemistry and isotopic characteristics of the eastern ore zone of the Baiyangping polymetallic ore district, northwestern Yunnan Province, China. J. Asian Earth Sci. 85, 140–153.
George, L.L., Cook, N.J., Ciobanu, C.L., 2016. Partitioning of trace elements in co-crystallized sphalerite - galena - chalcopyrite hydrothermal ores. Ore Geol. Rev. 77, 97–116.
Ghosh, S., Schauble, E.A., Couloume, G.L., Blum, J.D., Bergquist, B.A., 2013. Estimation of nuclear volume dependent fractionation of mercury isotopes in equilibrium liquid–vapor evaporation experiments. Chem. Geol. 336, 5–12.
Gleason, J.D., Blum, J.D., Moore, T.C., Polyak, L., Jakobsson, M., Meyers, P.A., Biswas, A., 2017. Sources and cycling of mercury in the paleo Arctic Ocean from Hg stable isotope variations in Eocene and Quaternary sediments. Geochim. Cosmochim. Acta

197, 245–262.
Grammatikopoulos, T.A., Valeyev, O., Roth, T., 2006. Compositional variation in Hg-bearing sphalerite from the polymetallic Eskay Creek deposit, British Columbia, Canada. Chem Erde-Geochem 66, 307–314.
Grasby, S.E., Sanei, H., Beauchamp, B., Chen, Z., 2013. Mercury deposition through the Permo–Triassic Biotic Crisis. Chem. Geol. 351, 209–216.
He, L.Q., Song, Y.C., Chen, K.X., Hou, Z.Q., Yu, F.M., Yang, Z.S., Wei, J.Q., Li, Z., Liu, Y.C., 2009. Thrust-controlled, sediment-hosted, Himalayan Zn-Pb-Cu-Ag deposits in the Lanping foreland fold belt, eastern margin of Tibetan Plateau. Ore Geol. Rev. 36, 106–132.
Hou, Z.Q., Zaw, K., Pan, G.T., Mo, X.X., Xu, Q., Hu, Y.Z., Li, X.Z., 2007. Sanjiang Tethyan metallogenesis in S.W. China: tectonic setting, metallogenic epochs and deposit types. Ore Geol. Rev. 31, 48–87.
Jiskra, M., Wiederhold, J.G., Bourdon, B., Kretzschmar, R., 2012. Solution speciation controls mercury isotope fractionation of Hg (II) sorption to goethite. Environ. Sci. Technol. 46, 6654–6662.
Kiyosu, Y., Krouse, H.R., 1990. The role of organic acid in the abiogenic reduction of sulfate and the sulfur isotope effect. Geochim. J. 24, 21–27.
Kritee, K., Blum, J.D., Johnson, M.W., Bergquist, B.A., Barkay, T., 2007. Mercury stable isotope fractionation during reduction of Hg(II) to Hg(0) by mercury resistant microorganisms. Environ. Sci. Technol. 41, 1889–1895.
Kritee, K., Barkay, T., Blum, J.D., 2009. Mass dependent stable isotope fractionation of mercury during mer mediated microbial degradation of monomethylmercury. Geochim. Cosmochim. Acta 73, 1285–1296.
Laffont, L., Sonke, J.E., Maurice, L., Hintelmann, H., Pouilly, M., Bacarreza, Y.S., Perez, T., Behra, P., 2009. Anomalous mercury isotopic compositions of fish and human hair in the Bolivian Amazon. Environ. Sci. Technol. 43, 8985–8990.
Laffont, L., Sonke, J.E., Maurice, L., Monrroy, S.L., Chincheros, J., Amouroux, D., Behra, P., 2011. Hg speciation and stable isotope signatures in human hair as a tracer for dietary and occupational exposure to mercury. Environ. Sci. Technol. 45, 9910–9916.
Lamborg, C.H., Tseng, C.M., Fitzgerald, W.F., Balcom, P.H., Hammerschmidt, C.R., 2003. Determination of the mercury complexation characteristics of dissolved organic matter in natural waters with “reducible Hg” titrations. Environ. Sci. Technol. 37, 3316–3322.
Lan, T.G., Hu, R.Z., Bi, X.W., Mao, G.J., Wen, B.J., Liu, L., Chen, Y.H., 2018. Metasomatized asthenospheric mantle contributing to the generation of Cu-Mo deposits within an intracontinental setting: a case study of the ~128 Ma Wangjiazhuang Cu-Mo deposit, eastern North China Craton. J. Asian Earth Sci. 160, 460–489.
Leach, D.L., Sangster, D.F., Kelley, K.D., Large, R.R., Garven, G., Allen, C.R., Gutzmer, J., Walters, S., 2005. Sediment-hosted lead–zinc deposits: a global perspective. In: Hedenquist, J.W., Thompson, J.F.H., Goldfarb, R.J., Richards, J.P. (Eds.), Economic Geology 100th Anniversary, pp. 561–607 Volume.
Leach, D.L., Song, Y.C., Hou, Z.Q., 2017. The world-class Jinding Zn–Pb deposit: ore formation in an evaporite dome, Lanping Basin, Yunnan, China. Mineral. Deposita 52, 281–296.
Lu, H.Z., Fan, H.R., Ni, P., Ou, G.X., Shen, K., Zhang, W.H., 2004. Fluid Inclusion. Science Press, Beijing (in Chinese).
Machel, H., Krouse, H., Sassen, R., 1995. Products and distinguishing criteria of bacterial and thermochemical sulfate reduction. Appl. Geochem. 10, 373–389.
Motta, L.C., Chien, A.D., Rask, A.E., Zimmerman, P.M., 2020. Mercury magnetic isotope effect: a plausible photochemical mechanism. J. Phys. Chem. A 124, 3711–3719.
Percival, L.M.E., Witt, M.L.I., Mather, T.A., Hermoso, M., Jenkyns, H.C., Hesselbo, S.P., Al-Suwaidi, A.H., Storm, M.S., Xu, M., Ruhl, M., 2015. Globally enhanced mercury deposition during the end-Pliensbachian extinction and Toarcian OAE: a link to the Karoo–Ferrar Large Igneous Province. Earth Planet. Sci. Lett. 428, 267–280.
Roedder, E., 1984. Fluid inclusions. Rev. Mineral. 12, 644.
Sanei, H., Grasby, S.E., Beauchamp, B., 2012. Latest Permian mercury anomalies. Geology 40, 63–66.
Schauble, E.A., 2007. Role of nuclear volume in driving equilibrium stable isotope fractionation of mercury, thallium, and other very heavy elements. Geochim. Cosmochim. Acta 71, 2170–2189.
Shen, J., Algeo, T.J., Chen, J.B., Planavsky, N.J., Feng, Q.L., Yu, J.X., Liu, J.L., 2019. Mercury in marine Ordovician/Silurian boundary sections of South China is sulfide-hosted and non-volcanic in origin. Earth Planet. Sci. Lett. 511, 130–140.
Sheng, X.Y., Bi, X.W., Hu, R.Z., Tang, Y.Y., Lan, Q., Xiao, J.F., Tao, Y., Huang, M.L., Peng, J.T., Xu, L.L., 2019. The mineralization process of the Lanuoma Pb-Zn-Sb deposit in the Sanjiang Tethys region: constraints from in situ sulfur isotopes and trace element compositions. Ore Geol. Rev. 111, 102941.
Sherman, L.S., Blum, J.D., Nordstrom, D.K., McCleskey, R.B., Barkay, T., Vetriani, C., 2009. Mercury isotopic composition of hydrothermal systems in the Yellowstone Plateau volcanic field and Guaymas Basin sea-floor rift. Earth Planet. Sci. Lett. 279, 86–96.
Smith, C.N., Kesler, S.E., Klaue, B., Blum, J.D., 2005. Mercury isotope fractionation in fossil hydrothermal systems. Geology 33, 825–828.
Smith, C.N., Kesler, S.E., Blum, J.D., Rytuba, J.J., 2008. Isotope geochemistry of mercury in source rocks, mineral deposits and spring deposits of the California Coast Ranges, USA. Earth Planet. Sci. Lett. 269, 399–407.
Smith, R.S., Wiederhold, J.G., Kretzschmar, R., 2015. Mercury isotope fractionation during precipitation of metacinnabar (β-HgS) and montroydite (HgO). Environ. Sci. Technol. 49, 4325–4334.
Sonke, J.E., 2011. A global model of mass independent mercury stable isotope fractionation. Geochim. Cosmochim. Acta 75, 4577–4590.
Sonke, J.E., Schäfer, J., Chmeleff, J., Audry, S., Blanc, G., Dupré, B., 2010. Sedimentary mercury stable isotope records of atmospheric and riverine pollution from two major European heavy metal refineries. Chem. Geol. 279, 90–100.
Studley, S.A., Ripley, E.M., Elswick, E.R., Dorais, M.J., Fong, J., Finkelstein, D., Pratt, L.M., 2002. Analysis of sulfides in whole rock matrices by elemental analyzer–continuous flow isotope ratio mass spectrometry. Chem. Geol. 192, 141–148.
Sun, G.Y., Sommar, J., Feng, X.B., Lin, C.J., Ge, M.F., Wang, W.G., Yin, R.S., Fu, X.W., Shang, L.H., 2016. Mass-dependent and -independent fractionation of mercury isotope during gas-phase oxidation of elemental mercury vapor by atomic Cl and Br. Environ. Sci. Technol 50, 9232–9241.
Tang, Y.Y., Bi, X.W., Fayek, M., Hu, R.Z., Wu, L.Y., Zou, Z.C., Feng, C.X., Wang, X., 2014. Microscale sulfur isotopic compositions of sulfide minerals from the Jinding Zn-Pb deposit, Yunnan Province, Southwest China. Gondwana Res. 26, 594–607.
Tang, Y.Y., Bi, X.W., Yin, R.S., Feng, X.B., Hu, R.Z., 2017. Concentrations and isotopic variability of mercury in sulfide minerals from the Jinding Zn-Pb deposit, Southwest China. Ore Geol. Rev. 90, 958–969.
Them, T.R., Jagoe, C.H., Caruthers, A.H., Gill, B.C., Grasby, S.E., Gröcke, D.R., Yin, R.S., Owens, J.D., 2019. Terrestrial sources as the primary delivery mechanism of mercury to the oceans across the Toarcian Oceanic Anoxic Event (Early Jurassic). Earth Planet. Sci. Lett. 507, 62–72.
Thibodeau, A.M., Ritterbush, K., Yager, J.A., West, A.J., Ibarra, Y., Bottjer, D.J., Berelson, W.M., Bergquist, B.A., Corsetti, F.A., 2016. Mercury anomalies and the timing of biotic recovery following the end-Triassic mass extinction. Nat. Geosci. 7, 11147.
Varekamp, J.C., Buseck, P.R., 1984. The speciation of mercury in hydrothermal systems, with applications to ore deposition. Geochim. Cosmochim. Acta 48, 177–185.
Wang, X.H., Hou, Z.Q., Song, Y.C., Zhang, H.R., 2015. Geological, fluid inclusion and isotopic studies of the Baiyangping Pb–Zn–Cu–Ag polymetallic deposit, Lanping basin, Yunnan province, China. J. Asian Earth Sci. 111, 853–871.
Wang, X.D., Cawood, P.A., Zhao, H., Zhao, L.S., Grasby, S.E., Chen, Z.Q., Zhang, L., 2019. Global mercury cycle during the end-Permian mass extinction and subsequent Early Triassic recovery. Earth Planet. Sci. Lett. 513, 144–155.
Wiederhold, J.G., Cramer, C., Daniel, K., Infante, I., Bourdon, B., Kretzschmar, R., 2010. Equilibrium mercury isotope fractionation between dissolved Hg(II) species and thiol-bound Hg. Environ Sci Technol 44, 4191–4197.
Xu, C.X., 2017. Geochemical Features and Ore Genesis of Sediment-hosted Lead-Zinc Deposits in the Changdu Area, Tibet - Exemplified by Lanuoma and Cuona Pb-Zn Deposits. [Ph.D. thesis]. Institute of Geochemistry. Chinese Academy of Sciences, Guiyang, China (in Chinese with English abstract).
Xu, C.X., Yin, R.S., Peng, J.T., Hurley, J.P., Lepak, R.F., Gao, J.F., Feng, X.B., Hu, R.Z., Bi, X.W., 2018. Mercury isotope constraints on the source for sediment-hosted lead-zinc deposits in the Changdu area, southwestern China. Mineral. Deposita 53, 339–352.
Xue, C.J., Zeng, R., Liu, S.W., Chi, G.X., Qing, H.R., Chen, Y.C., Yang, J.M., Wang, D.H., 2007. Geologic, fluid inclusion and isotopic characteristics of the Jinding Zn-Pb deposit, western Yunnan, South China: a review. Ore Geol. Rev. 31, 337–359.
Xue, C.J., Chi, G.X., Fayek, M., 2015. Micro-textures and in situ sulfur isotopic analysis of spheroidal and zonal sulfides in the giant Jinding Zn–Pb deposit, Yunnan, China: implications for biogenic processes. J. Asian Earth Sci. 103, 288–304.
Yalikun, Y., Xue, C.J., Dai, Z.J., Chi, G.X., Fayek, M., Symons, D., 2018. Microbial structures and possible bacterial sulfide fossils in the giant Jinding Zn-Pb deposit, Yunnan, SW-China: insights into the genesis of Zn-Pb sulfide mineralization. Ore Geol. Rev. 92, 61–72.
Yin, R.S., Feng, X.B., Shi, W.F., 2010. Application of the stable-isotope system to the study of sources and fate of Hg in the environment: a review. Appl. Geochem. 25, 1467–1477.
Yin, R.S., Feng, X.B., Li, Z.G., Zhang, Q., Bi, X.W., Li, G.H., Liu, J.L., Zhu, J.J., Wang, J.X., 2012. Metallogeny and environmental impact of Hg in Zn deposits in China. Appl. Geochem. 27, 151–160.
Yin, R.S., Feng, X.B., Meng, B., 2013. Stable mercury isotope variation in rice plants (Oryza sativa L.) from the Wanshan mercury mining district, SW China. Environ Sci Technol 47, 2238–2245.
Yin, R.S., Feng, X.B., Hurley, J.P., Krabbenhoft, D.P., Lepak, R.F., Hu, R.Z., Zhang, Q., Li, Z.G., Bi, X.W., 2016. Mercury isotopes as proxies to identify sources and environmental impacts of mercury in sphalerites. Sci. Rep. 6, 18686.
Zambardi, T., Sonke, J.E., Toutain, J.P., Sortino, F., Shinohara, H., 2009. Mercury emissions and stable isotopic compositions at Vulcano Island (Italy). Earth Planet. Sci. Lett. 277, 236–243.
Zhang, J.X., Wang, W.C., Wu, D.P., Lei, Y.A., Guo, G.L., Mei, P.L., 2009. Mineralization feature of lead and zinc deposits related with carbonate rock in Weixi-Puer ore belt in west Yunnan. Mineral Resources and Geology 23, 442–495 (in Chinese with English abstract).
Zhang, J.R., Wen, H.J., Qiu, Y.Z., Zhang, Y.X., Li, C., 2013. Ages of sediment-hosted Himalayan Pb–Zn–Cu–Ag polymetallic deposits in the Lanping basin, China: Re–Os geochronology of molybdenite and Sm–Nd dating of calcite. J. Asian Earth Sci. 73, 284–295.
Zhang, J.R., Wen, H.J., Qiu, Y.Z., Zou, Z.C., Du, S.J., Wu, S.Y., 2015. Spatial-temporal evolution of ore-forming fluids and related mineralization in the western Lanping basin, Yunnan Province, China. Ore. Geol. Rev. 67, 90–108.
Zheng, W., Hintelmann, H., 2009. Mercury isotope fractionation during photoreduction in natural water is controlled by its Hg/DOC ratio. Geochim. Cosmochim. Acta 73, 6704–6715.
Zheng, W., Hintelmann, H., 2010. Nuclear field shift effect in isotope fractionation of mercury during abiotic reduction in the absence of light. J. Phys. Chem. A 114, 4238–4245.
Zheng, W., Foucher, D., Hintelmann, H., 2007. Mercury isotope fractionation during volatilization of Hg(0) from solution into the gas phase. J. Anal. At. Spectrom. 22, 1097–1104.
Zhu, C.W., Tao, C.H., Yin, R.S., Liao, S.L., Yang, W.F., Liu, J., Barriga, F.J.A.S., 2020. Seawater versus mantle sources of mercury in sulfide-rich seafloor hydrothermal systems, Southwest Indian Ridge. Geochim. Cosmochim. Acta 281, 91–101.
Zou, Z.C., Hu, R.Z., Bi, X.W., Wu, L.Y., Feng, C.X., Tang, Y.Y., 2015. Absolute and relative dating of Cu and Pb-Zn mineralization in the Baiyangping area, Yunnan Province, SW China: Sm-Nd geochronology of calcite. Geochem. J. 49, 103–112.